

Chapter 6

A PANCHROMATIC VIEW OF AGN

Guido Risaliti & Martin Elvis

Harvard-Smithsonian Center for Astrophysics

60 Garden Street, Cambridge, MA 02138

grisaliti,melvis@cfa.harvard.edu

Abstract We review the continuum emission of Active Galactic Nuclei (AGN) over the entire electromagnetic spectrum. After a brief historical introduction, we describe the main spectral properties of unobscured AGN, discussing the selection biases which prevent us from having a complete view of the AGN population in the universe, and trying to build an updated spectral energy distribution of optically selected quasars. In the second part of the review, we describe the spectral properties of obscured AGN. Finally, we discuss the main observational methods in the different wavelength bands for disentangling AGN and stellar emission, and the ability of these methods to find new (mainly obscured) AGN, a significant fraction of which are probably still missing in current surveys.

6.1 Introduction

Active Galactic Nuclei (AGN) shine over ~ 20 decades of the electromagnetic spectrum, from the radio to the gamma rays. In almost all of this huge energy range, AGN are the brightest sources in the sky, except for the relatively narrow (~ 3 decades) range from the infrared to the ultraviolet (UV).

The “modern history” of quasars is closely linked with the development of non-optical astronomy. In the early 60s, hard won precise positions of radio sources enabled the large optical telescopes of the day to take spectra of whatever optical object lay at that position. Some showed the starlight of normal galaxies, but often at large distances. In 1963 Marteen Schmidt made the “official” discovery of the first quasar, 3C 273, realizing that the point-like counterpart of a powerful radio source was at a redshift $z = 0.16$, implying an enormous luminosity. In

the early sixties, the availability of new space-borne instruments also opened the new field of astronomical observations in the X-rays, which soon revealed a sky dominated by AGN.

It is now clear that the initial population of quasars discovered in radio surveys is only a small fraction of a 10 times more numerous class of quasars, most of which are “radio quiet”. These sources are, in turn, a small fraction of the total AGN population, which is dominated by obscured sources that can only be detected through their hard X-ray emission or through their reprocessed radiation in the infrared.

In this chapter, we describe the main continuum properties of AGN across the whole electromagnetic spectrum, according to our present, still incomplete, knowledge. We do not treat the emission of the small minority of quasars known as “blazars”, whose emission appears significantly altered by relativistic beaming effects. We focus on the *observed* properties of quasars from a phenomenological point of view. More emphasis on the physical processes responsible for the observed emission of quasars can be found in Armitage (this volume).

We start in §6.2 with unobscured (type I) AGN. We briefly discuss the main limitations in defining a representative sample of AGN. We then focus on a sample of bright, optically selected quasars (the Bright Quasar Survey, Schmidt & Green 1983) in order to build a mean Spectral Energy Distribution (SED) that takes into account all of the most recent observational results. This can be considered an update of the 10 year old compilation of Elvis et al. (1994; hereafter, E94). We conclude §6.2 with a brief overview of the possible dependence of the average spectral properties of type I AGN on redshift and/or luminosity and with a brief discussion on the often underestimated issue of the intrinsic dispersion of quasar spectra with respect to their average shapes.

Section 6.3 is devoted to obscured (type II) AGN. We first review the main spectral properties for each energy band. We then discuss the relation between dust and gas absorption, describing some recently discovered sources for which the ratio between gas and dust, and the dust properties, are strongly different from those in our Galaxy. Finally, in §6.4 we discuss the current methods that can be used to discover obscured AGN in the different energy bands. There are several indications that a significant fraction of these sources are still missing in current surveys. In particular, we focus on the techniques that can help to disentangle the AGN and stellar emission in the population of luminous sources that dominate the infrared and submillimeter sky. We conclude with a brief summary in §6.5.

We finish this introduction with a note on terminology: historically, the term “quasar” has been used widely to refer to AGN of high lumi-

osity whose emission completely overwhelmed that of the host galaxy. (Thus, these sources appeared as point sources in optical observations.) Low-luminosity AGN were (and still are) referred to as “Seyfert Galaxies”. However, evidence for any basic physical difference between these types of active objects has diminished through the years, essentially to the vanishing point. For this reason, in this chapter, we will use the term “quasar” as synonymous with type 1 AGN.

6.2 Spectral Properties of Quasars

Defining the SED of quasars is an extremely difficult task from an observational point of view. This is mainly due to observational biases introduced by the narrow wavelength ranges used for the selection of all quasar samples.

Historically, the most common technique for quasar selection has been the UV-blue excess in the quasar continuum. For example, the best-studied quasar sample, the Bright Quasar Survey sample (part of the Palomar-Green survey, Schmidt & Green 1983, and hereafter referred to as “PG quasars”), is defined through a magnitude limit ($B < 16.2$, $M_V < -23$) and a color limit ($U - B < -0.4$). Detailed studies of this sample of quasars revealed a remarkable homogeneity in their continua (Sanders et al. 1989; E94) and line properties from the infrared to the X-rays (Laor et al. 1997), with the exception of a small fraction ($\sim 10\%$) of Broad Absorption Line (BAL) objects with quite different continua and line properties. Subsequent quasar samples have been obtained with deeper surveys but similar selection criteria.

However, the blue selection method is in no way complete and can provide only a partial view of the general quasar SED. This is evident in Figure 6.1, which shows the location of quasars from the Anglo-Australian Telescope’s Two Degree Field (2dF) QSO Redshift Survey (Croom et al. 2002) in the ($B - V$, $U - B$) plane. The “classical” UV excess selection criterion (*horizontal line*) was chosen for efficiency (selecting objects that are quasars) and not for completeness (selecting all quasars). Hence, the selection limit is in no way related to any intrinsic property of the quasars, but rather to the UV emission of stars: the color limit is chosen in order to reject the great majority of stars and thus have a high efficiency in quasar selection. In principle, a more relaxed color selection would find more quasars, but the fraction of stars among the selected objects would be much higher, making the spectroscopic follow-up extremely time-consuming.

Many other criteria have been adopted in order to increase the completeness. At other wavelengths, radio surveys like the Very Large Array

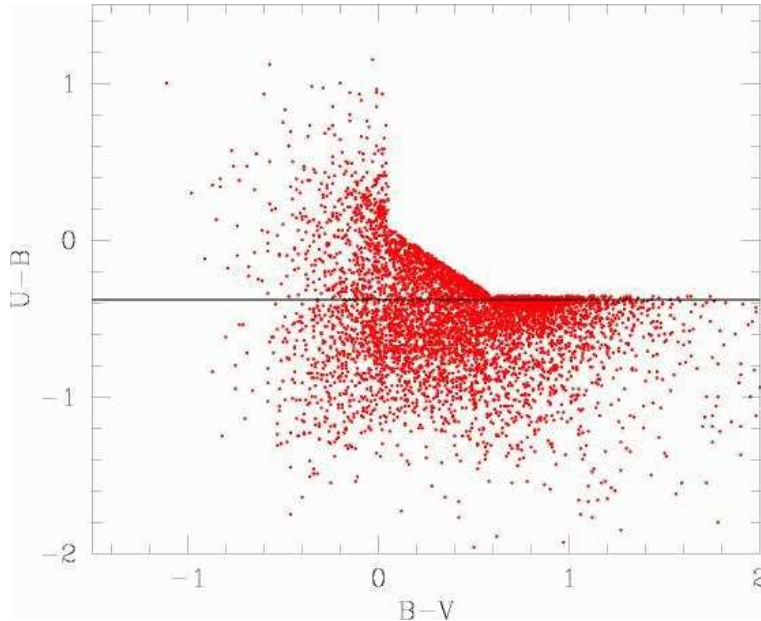


Figure 6.1. Color-color diagram for 2dF quasars. Horizontal line shows the “classical” selection criterion for blue quasars ($U - B < -0.4$). Empty region in the upper right is dominated by stars, and has therefore been excluded in the 2dF quasar search.

(VLA)’s Faint Images of the Radio Sky at Twenty-cm (FIRST) Bright Quasar Survey (White et al. 2000) are now deep enough to find “radio-quiet” objects (which are much fainter than radio-loud quasars at radio wavelengths, but are still detectable). X-ray surveys are also effective at discovering AGN that would be missed in optical searches because of their red colors or because of absorption (Brusa et al. 2003; Barger et al. 2003). In the optical band, spectroscopic criteria have been used to discover quasars from their broad emission lines instead of their continuum properties, e.g., the Palomar-Gris survey (Schneider et al. 1994), the Hamburg Quasar Survey (Hagen et al. 1995), and the Hamburg-ESO survey (Wisotzki et al. 1997). Finally, multicolor optical selections have been used in recent surveys, like the Sloan Digital Sky Survey (SDSS).

In the following, we will focus on blue-selected quasars in order to build a quasar SED. The reason for this choice is twofold: (i) blue-selected quasars are currently the best-studied, i.e., the ones with the best available multiwavelength observational data, and (2) their emission is thought to be representative of the *intrinsic* emission of most quasars. The cases for intrinsically different SEDs and for absorbed objects will be discussed later.

The standard reference for quasar SEDs is the atlas of E94, who collected observations of bright quasars from radio to hard X-ray wavelengths. The mean SED from this work is often cited as the “standard” quasar SED, and the main properties of this SED are in good agreement with the SEDs of optically selected quasars, such as the PG quasars. However, even within this sample, the 90% range of SEDs spans factors of ~ 10 or more at most frequencies. There are three main limitations to the E94 atlas:

- 1) *Selection criterion.* The E94 sample is defined by requiring the presence of a detection sufficient to yield a spectrum in an *Einstein Observatory* X-ray observation. As discussed in E94, this introduces a well known bias towards X-ray bright objects. For comparison, the average optical-to-X-ray flux ratio index¹, α_{OX} , is 1.35 for the E94 sample and 1.55 for the low redshift PG quasars (Laor et al. 1997), corresponding to a factor of 3 higher X-ray emission in the E94 sample.
- 2) *Lack of data.* The E94 sample did not have data in the range between the Lyman edge (13.2 eV) and the soft X-rays (0.2 – 0.4 keV).
- 3) *Limited number of quasars.* The E94 sample had 29 radio-quiet quasars and 18 radio-loud.

The first two points can now be addressed well, and a significant improvement is also possible for the third point. It is possible to quantitatively discuss the effects of the first point using observations at different wavelengths to estimate the correct ratios between the emissions in the different bands. Regarding the second point, a big part of the gap between the Lyman edge and the soft X-rays can now be filled, thanks to the availability of *Hubble Space Telescope (HST)* and *Far Ultraviolet Spectroscopic Explorer (FUSE)* UV spectra of high redshift quasars.

In the following, we build an average SED using mainly—but not only—the best studied quasars, i.e., the local ($z < 0.4$) PG quasars ($B < 16.2$, $U - B < -0.4$). We adopt a slightly different approach with respect to E94: in order to produce a final average SED, we work out the average spectrum in each observational band, and then we estimate the bolometric corrections for each spectral region. We make use of the latest observational results, in particular, those from the *Infrared Space Observatory (ISO)* in the infrared (Haas et al. 2001), *HST* in the UV

¹ α_{OX} is defined as the slope of a nominal power law connecting the continuum at 2500 Å with that at 2 keV ($\alpha_{OX} = 0.385 \times \log(f(2500\text{Å})/f(2 \text{ keV}))$)

for quasars (Telfer et al. 2002) and bright, lower luminosity Seyfert 1 galaxies (Crenshaw et al. 1999), and *ROSAT*, *BeppoSAX*, and *ASCA* in the X-rays (Laor et al. 1997; Mineo et al. 2000; George et al. 2000).

6.2.1 Optical/UV

The optical to UV emission of quasars is characterized by the “big blue bump” (Shields 1978; Malkan & Sargent 1982; Elvis 1985), where the peak of quasar emission is usually found. The peak energy is around the Lyman edge ($\lambda = 1216 \text{ \AA}$), and the spectrum can be well approximated with a power law both at lower and higher frequencies. Recent observations performed with *HST* of over 200 quasars (compiled by Telfer et al. 2002) provide a good quality mean spectrum from $\lambda \sim 300 \text{ \AA}$ to $\lambda \sim 3000 \text{ \AA}$. Composite spectra (see Fig. 6.2) extending from $\lambda \sim 1200 \text{ \AA}$ to $\lambda \sim 9000 \text{ \AA}$ have been obtained using data from ground-based optical surveys like the UK Schmidt Telescope’s Large Bright QSO Survey (Francis et al. 1991), the 2dF (Croom et al. 2002), the optical follow-up of the FIRST radio survey (Brotherton et al. 2001), and the SDSS (Vanden Berk et al. 2001). The SDSS includes more than 2200 spectra at redshifts between 0 and ~ 5 , providing the most accurate average optical spectrum of quasars so far, with a spectral resolution of a few \AA . In the overlapping band ($\sim 1200 - 3800 \text{ \AA}$), the *HST* and SDSS results match within the errors, providing a complete quasar spectrum in the 300 – 9000 \AA band. The main results of these studies are the following:

- The 300 – 5000 \AA continuum can be modeled with two power laws with slopes² $\alpha_1 = -1.76$ between 300 \AA and $\sim 1200 \text{ \AA}$ and $\alpha_2 = -0.44$ between 1200 \AA and 5000 \AA . At longer wavelengths, the spectrum appears to flatten significantly, but this effect is probably due to the contribution of galactic emission in the quasar spectra (see Vanden Berk et al. 2001 for more details).

- No correlation between optical continuum properties and redshift or luminosity has been found. An anticorrelation between the equivalent width (EW) of the main emission lines and the luminosity (the “Baldwin effect”, Baldwin 1977) has been found.

- Hundreds of emission lines are present in quasar spectra (a compilation of the brightest ones is given in Table 6.1). In addition to these lines, another major feature in the optical/UV spectra of quasars is the “small blue bump” (Wills, Netzer, & Wills 1985; Elvis 1985) between

²Somewhat different conventions are used for the power law index: photon index Γ in the X-rays ($\text{counts/sec/keV} \propto E^{-\Gamma}$), α in the radio ($f_\nu \propto \nu^\alpha$), and $-\alpha$ or α_λ in the optical. In this review, we follow the radio convention, as it is mathematically correct in the $\log f_\nu$ versus ν space.

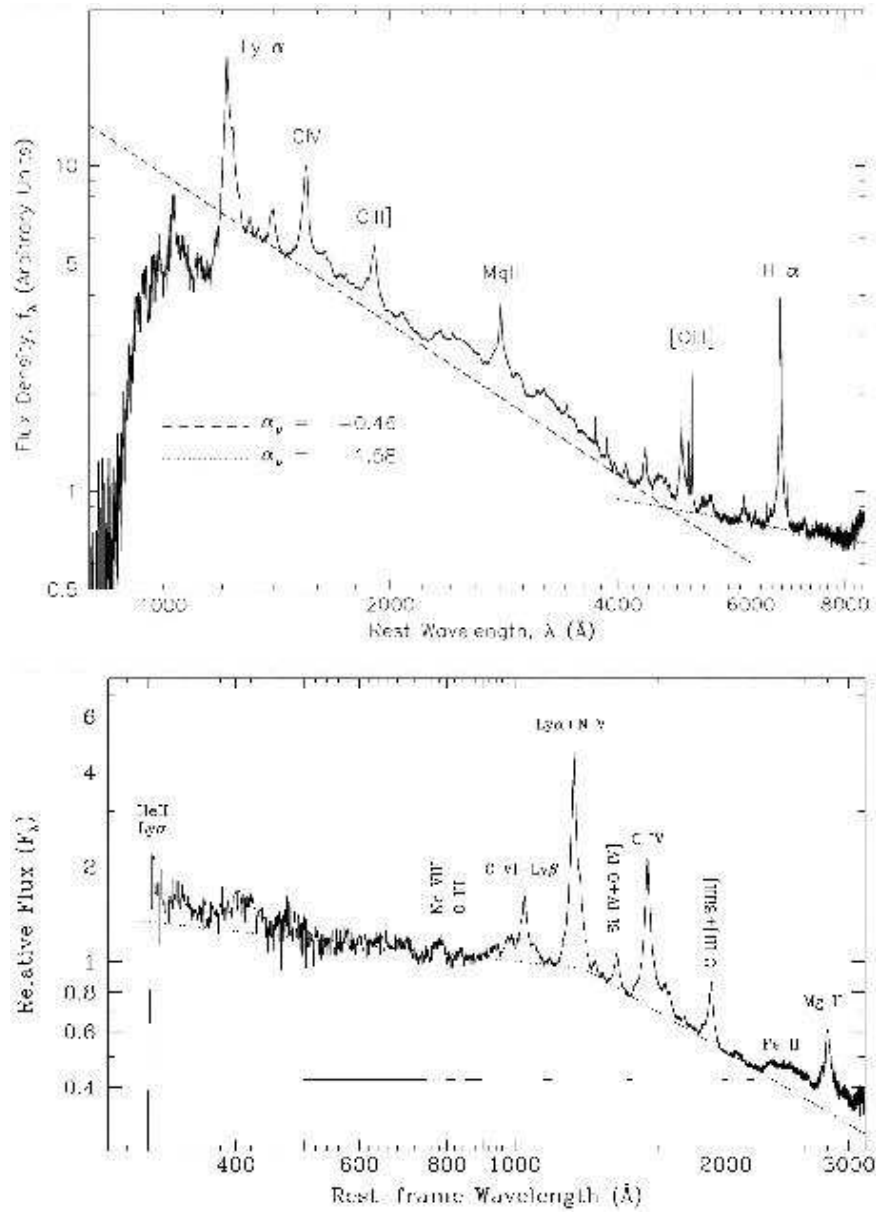


Figure 6.2. Composite optical/UV spectra of quasars. (*Upper panel*) Results from the SDSS (Vanden Berk et al. 2001; their Fig. 3). (*Lower panel*) Results from *HST* (Telfer et al. 2002; their Fig. 4). Dotted and dashed lines are power law fits to the continuum. Horizontal thick lines in the lower panel show the spectral regions used to estimate the continuum level.

$\sim 2200 \text{ \AA}$ and $\sim 4000 \text{ \AA}$. This is not a true continuum feature but is due to a forest of emission lines from the ion FeII and the Balmer recombination continuum. Permitted emission lines are “broad” (corresponding to velocities of the emitting gas of $2000 - 15000 \text{ km s}^{-1}$), while forbidden lines are narrow (a few hundred km s^{-1}).

- A minority ($\sim 10 - 20\%$) of quasars show broad absorption lines, often saturated, with widths and blueshifts of several thousand km s^{-1} and peaks of $20,000 - 30,000 \text{ km s}^{-1}$.

- $\sim 50\%$ of bright Seyfert 1 galaxies observed in the UV with *HST* or *FUSE* show evidence of Narrow Absorption Lines (NAL), with widths of $\sim 1000 \text{ km s}^{-1}$, in the profiles of high ionization emission lines (OVI, CIV, Ly α). The presence of such features is strongly correlated with the presence of warm absorbers in the soft X-rays (see §6.2.4).

Table 6.1. Compilation of the emission lines with $\text{EW} > 5 \text{ \AA}$ in the optical/UV spectra of quasars

<i>Line</i>	$\lambda(\text{\AA})$	$\langle \text{EW}(\text{\AA}) \rangle$	<i>Ref.</i>	<i>Line</i>	$\lambda(\text{\AA})$	$\langle \text{EW}(\text{\AA}) \rangle$	<i>Ref.</i>
CIII+NIII	980	9.7 ± 0.2	(1)	MgII	2799	32.3 ± 0.1	(2)
OVI+Ly β	1030	15.6 ± 0.3	(1)	H δ	4103	5.05 ± 0.06	(2)
Ly α	1216	91.8 ± 0.7	(1)	H γ	4341	12.6 ± 0.1	(2)
N V	1240	18.5 ± 0.5	(1)	H β	4863	46.2 ± 0.2	(2)
SiIV+OIV]	1397	8.13 ± 0.09	(2)	[OIII]	5007	13.2 ± 0.2	(2)
CIV	1549	23.8 ± 0.1	(2) ^a	H α	6565	$194.5 \pm 0.$	(2)
CIII]	1909	21.2 ± 0.1	(2)				

References — (1) Telfer et al. 2002 (for lines at $\lambda < 1300 \text{ \AA}$); (2) Vanden Berk et al. 2001 (for $\lambda > 1300 \text{ \AA}$).

Table notes — ^aThis is the only line in the $1300 - 3000 \text{ \AA}$ range for which the two references above give discrepant values (Vanden Berk reports the $\text{EW}(\text{CIV}\lambda 1549) = 23.8 \pm 0.1$ reported).

6.2.2 Radio/submillimeter

The radio emission of PG quasars (Kellerman et al. 1989) is significantly different for radio-loud and radio-quiet sources. However, in all cases, the radio emission provides a negligible fraction of the bolometric luminosity. Here we only concentrate on the “core” emission, i.e., the flat spectrum, compact component that is physically distinct from the steep spectrum lobes (however, the angular resolution is not always good enough to separate these components). In radio-loud objects, a strong, non-thermal continuum extends from the radio to the far-infrared through the submillimeter, while in radio-quiet objects, the SED turns

over sharply in the far-infrared, with a slope $\alpha > 2.5$ indicative of dust, and the radio emission is only a negligible tail of this component.

6.2.3 Infrared

The infrared (IR) emission of PG quasars has been systematically studied with the *Infrared Astronomical Satellite* (*IRAS*; Sanders et al. 1989), and, more recently, with the *ISO* satellite (Haas et al. 2003). The latter work confirms the basic results of the former, while adding further details. The basic characteristics of the IR emission of quasars are the following:

- The integrated IR emission ($2 - 200\mu\text{m}$) is, on average, $\sim 30\%$ of the bolometric luminosity, with values in individual objects ranging from $\sim 15\%$ to $\sim 50\%$. The spectral shape is characterized by (i) a minimum at $\sim 1 - 2\mu\text{m}$, corresponding to the sublimation temperature of the most refractory dust (between 1000 and 2000 K, depending on the composition of the dust grains), (ii) an “IR bump”, typically at $10 - 30\mu\text{m}$ (but there are examples of flat spectra, or peaks anywhere between 2 and $100\mu\text{m}$), due to the thermal emission of dust, with a temperature range between 50 and 1000 K, and (iii) a steep decline ($f_\nu \propto \nu^\alpha, \alpha > 3$) at large wavelengths, typical of the low energy spectrum of a gray emitter (Chini et al. 1989).

- The spectral shape of most of the sources in the sample is better reproduced, according to Haas et al. (2003), by reprocessing of the quasar primary emission, with the contribution of a starburst being negligible. However, this is still a controversial point, since the IR continuum expected from a quasar or a starburst is strongly dependent on the geometric and physical properties of the reprocessing medium, and the same observed continuum can often be successfully explained with more than one model (Elitzur, Nenkova, & Ivezić 2004).

- The far-IR emission of radio-loud quasars is quite different than that of radio-quiet quasars. The spectrum between the IR bump and the submillimeter range is well reproduced by a power law with spectral index close to $\alpha = 2.5$, as expected from self-synchrotron absorption. The main emission mechanism here is not reprocessing by dust, but synchrotron emission by relativistic electrons.

6.2.4 X-rays

The X-ray properties of bright, optically selected quasars have been intensively studied in the last 25 years (Elvis et al. 1978; Zamorani et al. 1981), mostly with broadband but low resolution spectra. The X-ray emission from quasars extends from the Galactic absorption cut-off at \sim

0.1 keV up to ~ 300 keV. Laor et al. (1997) analyzed the *ROSAT* soft X-ray (0.5–2 keV) observations of the sample of local ($z < 0.4$) PG quasars, and a subsample of these objects has been studied with *ASCA* in the 2–10 keV band (George et al. 2000) and with *BeppoSAX* in the 1–100 keV band (Mineo et al. 2001). Recent studies of samples of bright Seyfert 1 galaxies are reported in George et al. (1997; *ASCA* observations) and in Perola et al. (2002; *BeppoSAX* observations). The main properties of the X-ray spectra of type I AGN are briefly summarized below and are shown in Figure 6.3.

- *Primary emission.* The intrinsic continuum X-ray emission of quasars is to first order a power law, extending from about 1 keV to over 100 keV. However, as higher resolution and better signal-to-noise spectra have become available, emission and absorption features have been found that mask a direct view of this “power law” over virtually the whole X-ray band (see Fig. 6.3). Hence, slight curvatures may be present but unseen. The typical spectral index³ is between $\alpha = -0.8$ and $\alpha = -1$, both for low luminosity Seyfert galaxies and high luminosity quasars. Radio-loud AGN have a somewhat flatter spectrum (α between -0.5 and -0.7). This is thought to be due to the additional hard component emitted by inverse-Compton scattering of the electron in the jet on the radio-synchrotron photons, but this is not fully established.

There is now increasing evidence, mostly from *BeppoSAX*, for a roughly exponential cut-off to the power law at energies $\sim 80 - 300$ keV. This is presumably due to the cut-off in the energy distribution of the electrons responsible for the X-ray emission. It is still debated whether the spectral index is redshift or luminosity dependent (Zamorani et al. 1981; Avni & Tananbaum 1982, 1986; Bechtold et al. 2002; Vignali et al. 2003).

In addition to the main power law continuum component, a soft emission component is often observed in AGN, with characteristic temperature $kT \sim 0.2 - 1$ keV. The physical origin of this component is not clear: warm emitting gas could be located in the accretion disk, or in the broad line region (it could be the confining medium of the broad emission line clouds), or in a region farther from the center. Alternatively, this “soft excess” could be an extension of the big blue bump to higher energies, e.g., via Compton scattering in a hot accretion disk corona (Czerny & Elvis 1987).

- *Reflection components.* The primary emission of AGN can be “reflected”, i.e., Thomson scattered by ionized gas. If the reflector has a

³X-ray astronomers tend to use the “photon index” Γ , where $N(E) \propto E^{-\Gamma}$ and $\alpha = -(\Gamma - 1)$.

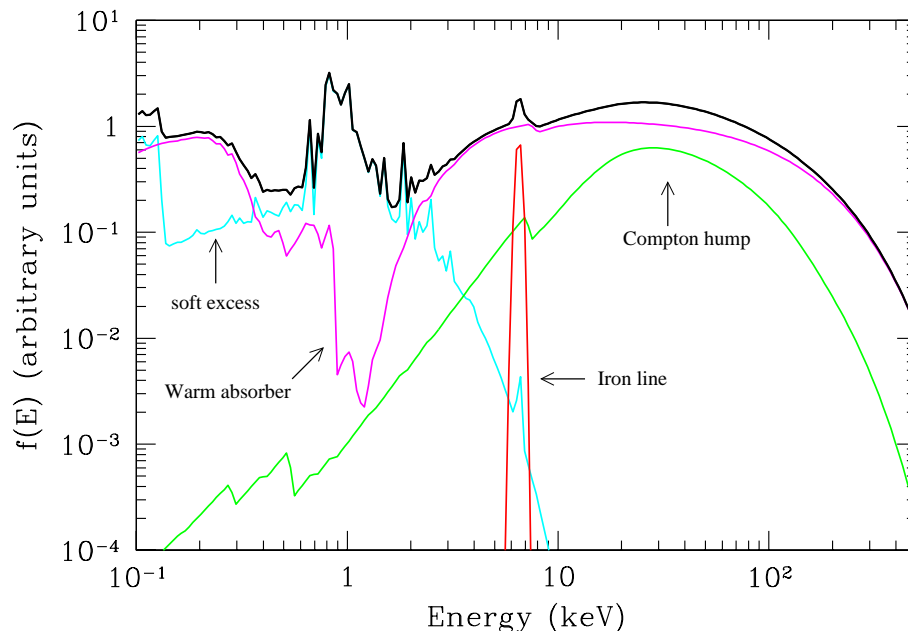


Figure 6.3. Average total spectrum (*thick black line*) and main components (*thin grey lines*) in the X-ray spectrum of a type I AGN. The main primary continuum component is a power law with an high energy cut-off at $E \sim 100\text{--}300$ keV, absorbed at soft energies by warm gas with $N_H \sim 10^{21} - 10^{23}$ cm $^{-2}$. A cold reflection component is also shown. The most relevant narrow feature is the iron $K\alpha$ emission line at 6.4 keV. Finally, a “soft excess” is shown, due to thermal emission of a Compton thin plasma with temperature $kT \sim 0.1 - 1$ keV.

column density $N_H > 1.5 \times 10^{24}$ cm $^{-2}$ (i.e., $\sim 1/\sigma_T$) and is not fully ionized, the reflected component has a spectrum like the one shown in Figure 6.3 (the actual shape slightly varies, depending on the geometry and chemical composition of the reflector). The main features of this reflection component are a continuum due to electron scattering with a peak at ~ 30 keV, and a cut-off at 4 – 5 keV due to photoelectric absorption of the lower energy incident radiation. The reflection efficiency is typically a few percent of the direct emission in the 2 – 10 keV range because of photoelectric absorption, rising to $\sim 30\%$ at the 30 keV peak for a Compton-thick reflector covering a significant fraction of the solid angle (Ghisellini et al. 1994). The efficiency drops if the reflecting medium is Compton thin (in this case part of the incident radiation escapes without interaction).

A warm, ionized reflector must be present in the central region of many AGN (since we see a “warm absorber” in $\sim 50\%$ of Seyfert 1 galax-

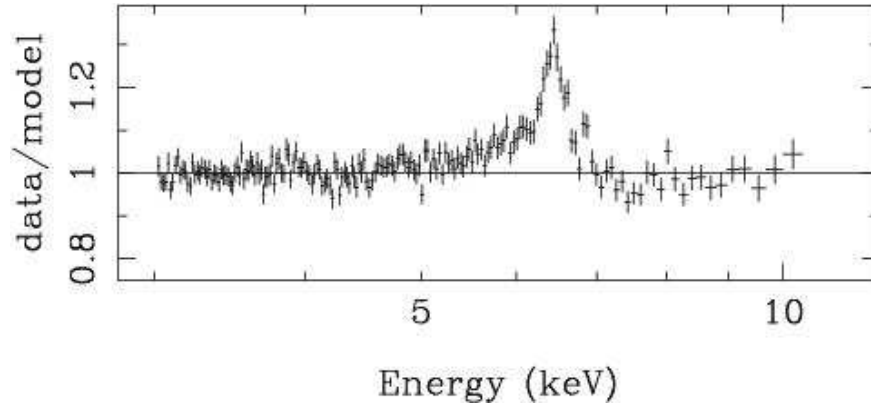


Figure 6.4. Iron line profile in an *XMM-Newton* observation of the Seyfert 1 galaxy MCG-6-30-15. Model is a power law fitted in the 3 – 5 keV and 8 – 10 keV energy bands. Figure is from Vaughan & Fabian (2004; their Fig. 8)

ies). The reflected emission has the same spectral shape as the incident continuum.

- *Iron line.* The most prominent narrow feature in the 2 – 10 keV X-ray spectra of AGN is an iron emission line at energy 6.4 keV, corresponding to the Fe-K $n = 2 - 1$ transition of “cold” (i.e., \leq FeXVII) iron. The line is usually ascribed to emission due to fluorescence in the inner part of the accretion disk. The typical EW of the line is 100 – 200 eV. There is also evidence for a broad “red wing” extending to lower energies (Tanaka et al. 1995; Nandra et al. 1997). Once thought to be widespread, *XMM-Newton* spectra now show signs of this red wing only in a few objects (MCG-6-30-15 being the clearest example, Vaughan & Fabian 2004; see Fig. 6.4). This red wing has caused great excitement as a likely physical cause is the gravitational redshift and relativistic Doppler shift of an Fe-K line originating from an accretion disk at only a few Schwarzschild radii (R_S) from the central black hole. Such a broad line would be one of the best tools to look for general relativistic effects in strong gravity. Asymmetric profiles have been calculated for lines emitted at a few Schwarzschild radii from non-rotating (Fabian et al. 1989) and rotating (Laor 1990) black holes.

A second, narrow component of the Fe-K line is very clearly present in most AGN. The width of this “narrow” line (which is unresolved in CCD spectra from *ASCA*, *Chandra* ACIS, or *XMM-Newton* EPIC) is a few 1000 km s⁻¹ or smaller when measured with the *Chandra* HETG spectrograph. This is similar to the width of optical and UV broad emission lines. This narrow component does not vary when the continuum varies,

even for delay times of days. Coupled with the line width, this suggests an origin well beyond a few R_S , although a small radius is not fully ruled out (Fabian et al. 2002). In the next few years, the *ASTRO-E2* satellite, with 6 eV resolution ($R = 1000$) and an effective area of $\sim 150 \text{ cm}^2$, is expected to do much better in understanding this issue. If the reflector is highly ionized, the peak energy of this line can be shifted toward high energies (6.7 keV for helium-like iron and 6.96 keV for hydrogen-like iron). It is also possible that two narrow components are present in the spectrum, one emitted by a cold reflector and the other by an ionized reflector. CCD detectors like the *ASCA* SIS or *XMM-Newton* EPIC (with energy resolution of $\sim 120 - 150 \text{ eV}$ at 6 keV) are unable to separate these two lines, while the *Chandra* HETG spectrograph has limited effective area ($\sim 40 \text{ cm}^2$) at 6 keV.

- *Warm absorbers.* Warm absorber features are present in the soft X-ray spectra of half of the bright Seyfert 1 galaxies observed with *ASCA* (Reynolds et al. 2000). Recently, the availability of high resolution soft X-ray spectra, obtained with the grating instruments onboard *Chandra* and *XMM-Newton*, show that this component is formed by an outflowing gas. We show in Figure 6.5 the highest signal-to-noise high resolution spectrum of an AGN, obtained with a long observation of the Seyfert 1 galaxy NGC 3783. Recently, Krongold et al. (2003) were able to reproduce all of the observed lines with a two-phase absorber, with the two phases in pressure equilibrium.

6.2.5 Bolometric Corrections

Given an intrinsic dispersion in the SED of quasars, any flux-limited sample selected in a given spectral band is biased towards high ratios between the flux in the selection band and the bolometric emission. This effect must be carefully taken into account in the construction of an AGN SED.

A well investigated example of the relevance of this selection effect is the average value of the optical-to-X-ray flux ratio $\langle \alpha_{OX} \rangle$ obtained in different quasar samples. E94 estimate $\langle \alpha_{OX} \rangle = -1.35$ for their X-ray selected sample. On the other hand, Laor et al. (1997) find $\langle \alpha_{OX} \rangle = -1.55$ for local, optically selected PG quasars. The difference, $\Delta \alpha_{OX} = 0.2$, is a factor of ~ 3.3 in the flux ratio. It is possible to use the distribution of observed α_{OX} in the two samples to estimate the effect of the selection bias. Elvis et al. (2002) showed that after this correction, the values estimated from the two samples match, with $\langle \alpha_{OX} \rangle = -1.43$. These corrections are important when estimating the accretion luminosity of

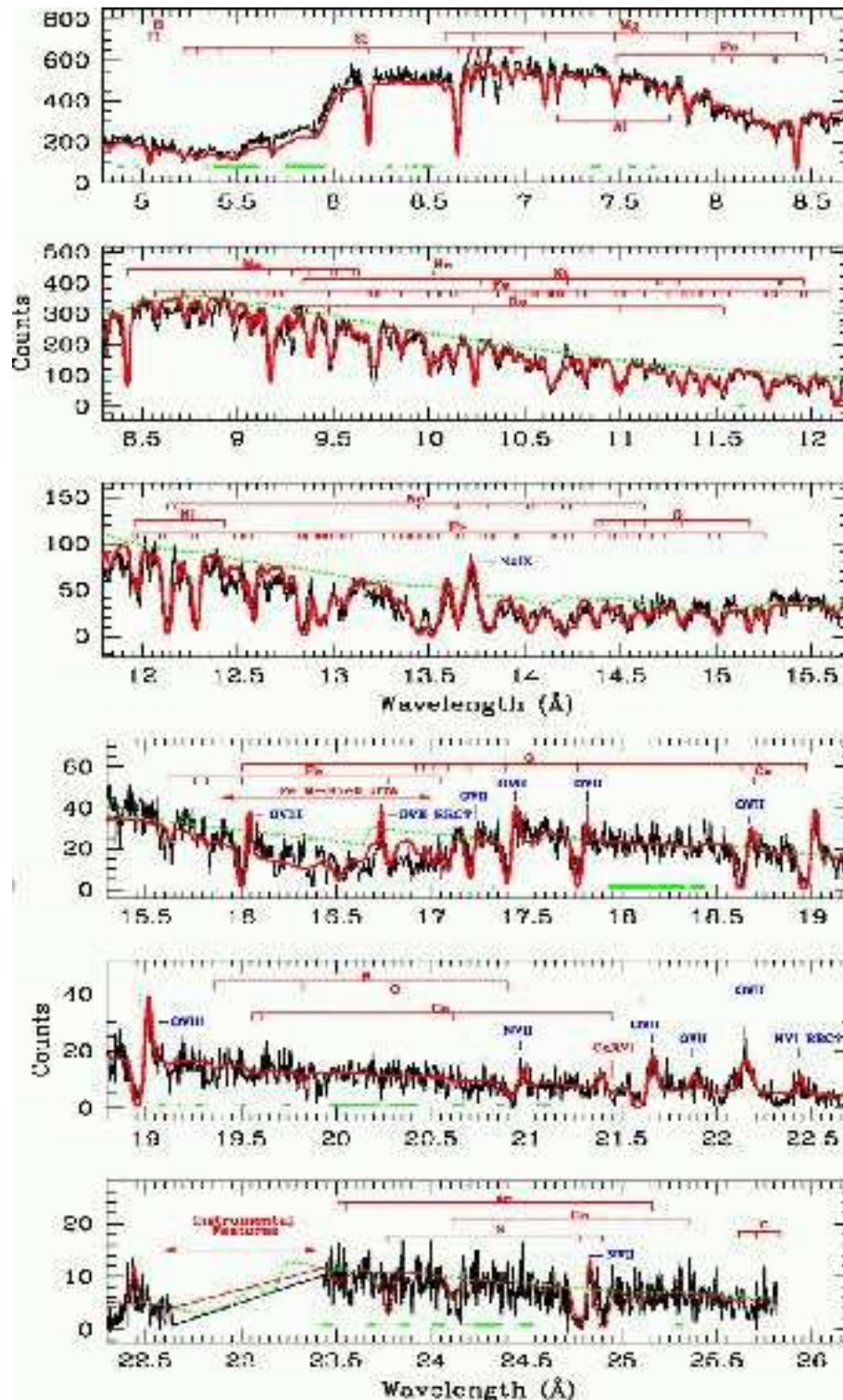


Figure 6.5. Chandra grating spectrum of NGC 3873, superimposed with a simple two-component model fitting most of the absorption features. Figure is from Krongold et al. (2003; their Fig. 3).

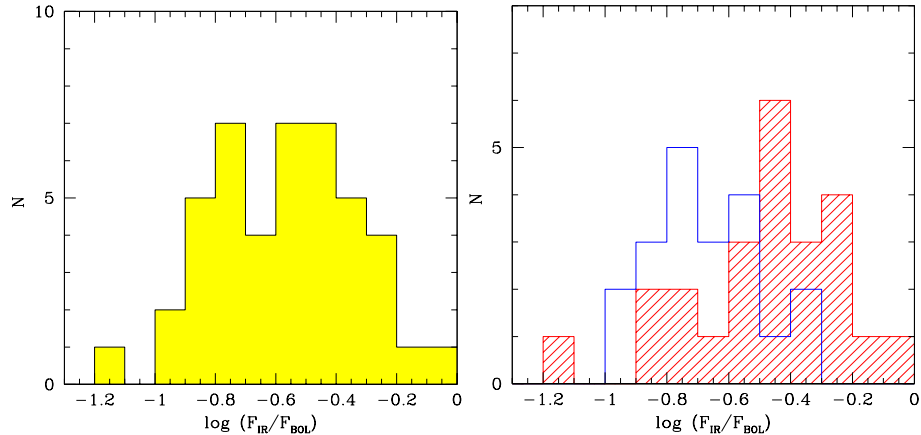


Figure 6.6. (a) Distribution of logarithmic IR-to-bolometric ratio for local ($z < 0.4$) PG quasars observed with *ISO* (Haas et al. 2003). (b) Same, for objects with luminosity $L_{IR} < 10^{12}$ ergs s^{-1} (empty histogram) and $L_{IR} > 10^{12}$ ergs s^{-1} (shaded histogram).

the universe and comparing this with the mass spectrum of local black holes (Fabian & Iwasawa 1999; Elvis, Risaliti, & Zamorani 2002).

The analogous correction has not been computed so far for the IR emission of PG quasars. We do this here. In Figure 6.6a, we plot the logarithmic ratio α_{IR} of the IR ($3 - 1000\mu\text{m}$) to $> 1\mu\text{m}$ (bolometric) emission for the $z < 0.4$ PG quasars observed with *ISO* (Haas et al. 2003). The emission from 2 to $100\mu\text{m}$ has been estimated from the *B*-band magnitude and the bolometric correction in E94. Approximating the distribution in Figure 6.6a with a Gaussian with a mean observed ratio $\langle\alpha_{IR}\rangle_{obs} = -0.56$ and $\sigma = 0.3$, one obtains that the average α_{IR} , corrected for the observational bias, is $\langle\alpha_{IR}\rangle = \langle\alpha_{IR}\rangle_{obs} + \sigma^2/2 = -0.51$. The corresponding fraction of the bolometric luminosity emitted in the IR is 31%.

A summary of the average contribution of several spectral bands to the bolometric emission of local quasars is shown in Table 6.2. In this compilation, we made use of the data discussed above on PG quasars, as well as *HST* data of optically selected quasars (Telfer et al. 2002). These data do not show any spectral dependence with redshift in the optical/UV and therefore are assumed to be representative of local quasars. The $1 - 3\mu\text{m}$ continuum, which is not covered in any of the works discussed above, has been taken from E94.

Table 6.2. Bolometric corrections for local quasars

<i>Band</i>	<i>Range (λ)</i>	<i>Range (ν)</i>	<i>Range (energy)</i>	<i>F/F_{TOT}</i>
Radio	3m-0.1mm	10^8 - 3×10^{11} Hz	4×10^{-7} – 1.2×10^{-3} eV	0%
Submillimeter	1000-150 μ m	3 - 20×10^{11} Hz	1.2 - 8.3×10^{-3} eV	0.2%
far-IR	150-40 μ m	2 - 7.5×10^{12} Hz	8.3 - 31×10^{-3} eV	4.9%
mid-IR	40-10 μ m	7.5 - 30×10^{12} Hz	3.1 - 12×10^{-2} eV	13.9%
mid-IR	10-3 μ m	3 - 10×10^{13} Hz	0.12-0.41 eV	11.9%
near-IR	3-1 μ m	1 - 3×10^{13} Hz	0.41-1.25 eV	7.0%
Opt	1 μ m-3000 Å	3 - 10×10^{14} Hz	1.25-4.16 eV	12.2%
UV	3000-1200 Å	1 - 2.5×10^{15} Hz	4.16-10.4 eV	16.5%
EUV ^a	1200-12.5 Å	2.5 - 240×10^{15} Hz	10.4 eV-1.0 keV	29.1%
X-ray	12.5-0.125 Å	2.4 - 240×10^{17} Hz	1-100 keV	4.2%

Table notes — ^aBased on high redshift quasars (Telfer et al. 2002).

6.2.6 Luminosity and Redshift Effects

The SED described above is representative of local, optically selected quasars. Here we summarize the evidence for luminosity or redshift dependence in the emission of quasars. The optical and UV spectra of quasars observed with *HST* and the SDSS show no evidence of a dependence on redshift or luminosity. On the other hand, the optical-to-X-ray ratio α_{OX} shows clear evidence of a luminosity or redshift dependence in optically selected samples (Zamorani et al. 1981; Avni & Tananbaum 1982, 1986; Wilkes et al. 1994; Yuan et al. 1998; Bechtold et al. 2002; Vignali et al. 2003). Yuan et al. (1998b) discussed the reality of this effect in the *ROSAT* sample and concluded that the luminosity and/or redshift dependence could be due to selection effects, provided that the intrinsic dispersion in the X-ray emission of quasars is greater than in the optical.

The latest results from the SDSS (Vignali et al. 2003), however, strengthen the observational evidence for a dependence. The statistical analyses performed on the SDSS quasars (Vignali et al. 2003) and on the sample of optically selected quasars observed with *ROSAT* (Yuan et al. 1998) suggest that the dependence is only on luminosity and not on redshift. However, it remains difficult to disentangle the dependence on redshift and luminosity, which are strongly correlated in flux-limited samples. In Figure 6.7, we show the α_{OX} -luminosity correlation for a sample of SDSS quasars observed (mostly serendipitously) with *ROSAT* and *Chandra* (Vignali et al. 2003). The best-fit linear correlation is $\alpha_{OX} = -0.11 \times \log L_{\nu}(2500 \text{ \AA}) + 1.85$.

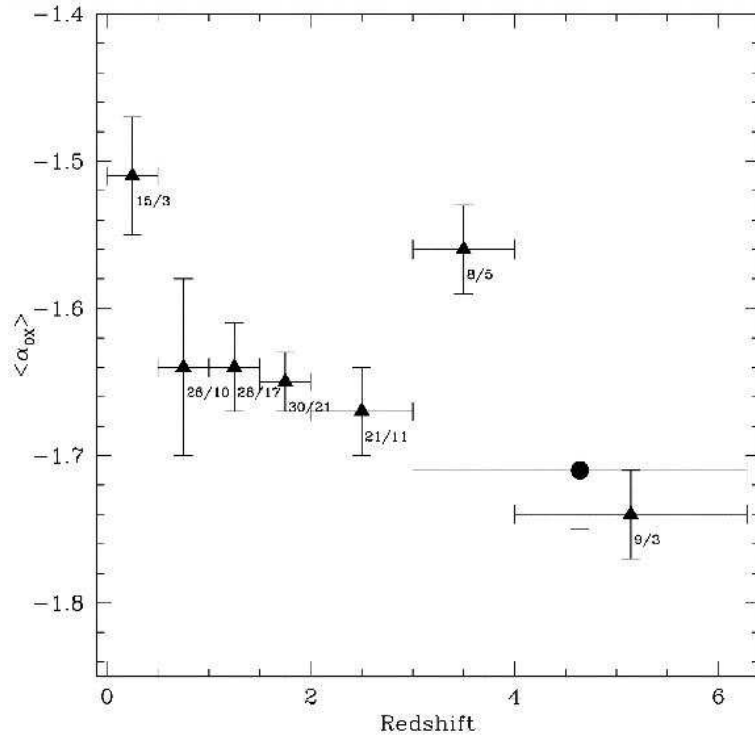


Figure 6.7. Dependence of α_{OX} on optical luminosity in SDSS quasars observed with *ROSAT*. Triangles are averages using the number of quasars indicated next to each point (*first number*—total number of quasars in the luminosity interval; *second number*—number of X-ray upper limits in the luminosity interval). Circle is an average using all quasars at redshifts $z > 3$. Figure from Vignali et al. (2003; their Fig. 7b).

The dependence of the IR emission of quasars on luminosity is much harder to estimate, mainly because of the possible contribution from star formation. In Figure 6.6b, we plot the distribution of the IR-to-bolometric ratio for the same sample as Figure 6.6a, but for two luminosity ranges: $L_{IR} < 3 \times 10^{12} L_{\odot}$ (*shaded histogram*) and $L_{IR} > 3 \times 10^{12} L_{\odot}$ (*open histogram*). Apparently, higher luminosity sources have, on average, a smaller fraction of their emission in the IR. Haas et al. (2003) concluded that most of the observed emission is due to the AGN. The same conclusion was reached by Kuraszkiwicz et al. (2003) for *ISO* SEDs of X-ray selected AGN. However, we cannot exclude the possibility that the effect in Figure 6.6b is due to a higher contamination by nuclear star formation in lower luminosity sources.

6.2.7 Intrinsic Dispersion

As we will point out later, different quasar selection criteria produce different SEDs. Even with an homogeneous selection, the dispersion in the SEDs of AGN is rather large, about an order of magnitude in the IR and UV, even when normalized at the $1\mu\text{m}$ “inflation point”. The dispersion in the SED of local X-ray selected quasars is emphasized in E94 and shown in Figure 6.8, but it is often not taken into account.

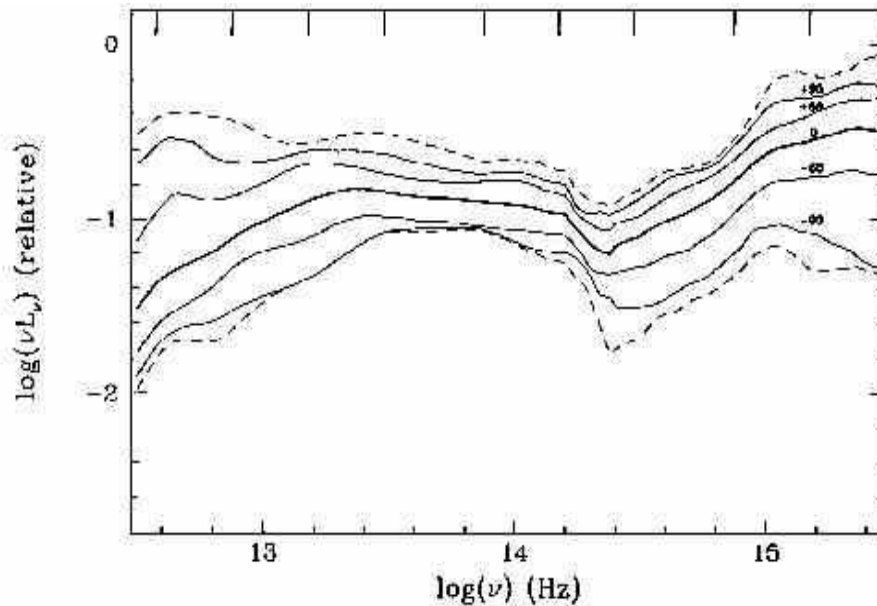


Figure 6.8. Intrinsic dispersion in the SED of E94. Curves represent the 99%, 90%, and 68% dispersion with respect to the best fit SED and are normalized in order to have the same flux at $1.25\ \mu\text{m}$.

We believe this dispersion to be a fundamental property of quasars that always should be considered when referring to an average SED. The reason is both “physical”, in order to have a physically correct view of quasar emission, and “computational”, since the results obtained when computing integral properties of quasar samples can be significantly altered by a non-zero dispersion distribution of parameters. An example is the correction from the observed to the “effective” α_{OX} discussed in §6.2.5.

We already discussed the dispersion in the IR emission in §6.2.7. Here we only note that, even if part of the observed dispersion (see Fig. 6.6) is due to a star formation contribution, it is likely that the intrinsic dispersion in the IR-to-bolometric ratio is a factor of ~ 2 . Finally, in Figure 6.9

we show the distribution of α_{OX} for the sample of optically selected quasars observed with *ROSAT* (Yuan et al. 1998). Approximating the distribution with a Gaussian, the standard deviation is $\sigma(\alpha_{OX}) \sim 0.2$, corresponding to a dispersion in the ratio between optical and X-ray emission of a factor of ~ 3 .

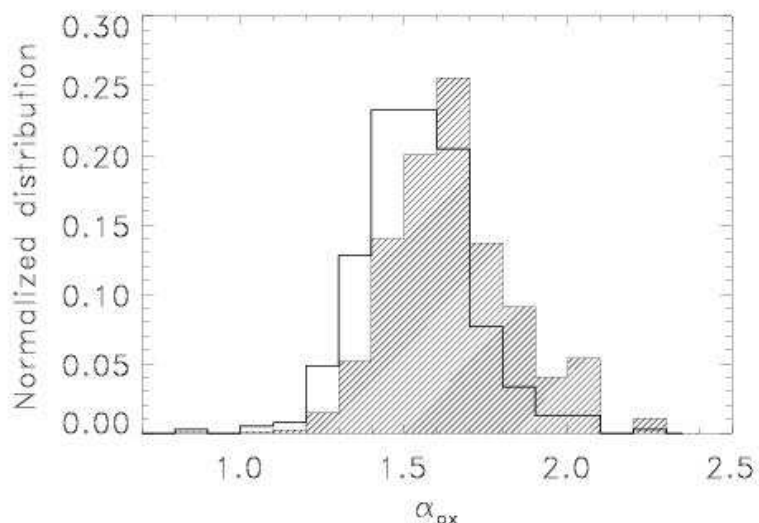


Figure 6.9. Distribution of α_{OX} for a sample of ~ 1000 optically selected quasars observed with *ROSAT*. Empty histogram shows the *ROSAT* detections; shaded histogram takes into account upper limits, as well. Figure from Yuan et al. (1998; their Fig. 9)

6.3 SEDs of Obscured AGN

Most of the AGN emission in the universe is obscured. Locally, optically obscured (“type II”) AGN outnumber unobscured AGN (“type I”) by a factor of ~ 4 (Maiolino & Rieke 1995). This factor could be even higher at redshifts $z = 0.5 - 1$, according to synthesis models of the X-ray background (Gilli et al. 2001). Absorption introduces a further spread in the emission properties of AGN, since the observed SEDs depend both on the intrinsic emission (which has a large dispersion) and on the amount, composition, and geometry of the absorber. In general, the main absorption mechanisms in AGN are the following:

(1) *Line absorption due to atomic transitions.* The strongest features observed in AGN spectra (“Narrow Absorption Lines” and “Broad Absorption Lines” in the UV, “Warm Absorption” in the soft X-rays) are mainly due to resonant absorption lines.

(2) *Continuum absorption in the IR to UV due to dust.*

(3) *Continuum absorption (or scattering) in the X-rays due to photoelectric absorption by dust and gas.*

The physical state (temperature, density), column density, and metallicity of the gas, the chemical composition of the dust, the dust-to-gas ratio, and the composition of the dust grains are all elements that affect the observed SED. Here we review the main emission properties of obscured AGN, focusing mostly on the actual observational results and only briefly discussing their physical interpretation.

6.3.1 Radio/IR

The radio emission properties of optically obscured AGN are similar to those of unobscured, type I AGN. A flat-spectrum, compact radio core is present in local AGN, with brightness temperatures $T_B > 10^5$ K. Recent VLA observations (Nagar et al. 2000) also revealed these radio cores in low luminosity ($L < 10^{41}$ ergs s⁻¹) AGN, showing that radio emission is an ubiquitous property of all AGN. However, the fraction of luminosity emitted in the radio band is in all cases negligible with respect to the bolometric luminosity.

In some cases, free-free absorption can alter the observed radio spectrum of an AGN covered by a compact layer of warm gas (Neufeld et al. 1994). At high radio luminosity, HI absorption is also common (Veron-Cetty et al. 2000). HI and/or free-free absorption is preferentially found in X-ray heavily absorbed (column density $N_H > 10^{24}$ cm⁻²), optically type II sources (Risaliti, Woltjer, & Salvati 2003b).

6.3.2 Near-IR/UV

The optical to UV band continuum emission is affected by dust absorption. Typically, the optical/UV continuum in type II AGN is heavily absorbed by dust and thermally reradiated at longer wavelengths. The observed continuum is dominated by the stellar contribution of the host galaxy and/or scattered emission. This latter component can be disentangled through observations in polarized light (see below for further details).

The emission-line spectrum is dominated by “narrow” emission lines (typical widths $300 - 800 \text{ km s}^{-1}$) corresponding to forbidden atomic transitions plus Balmer lines. This implies that the emitting gas is located farther from the center than the broad emission line emitter (if the width is interpreted as Keplerian motion) and that its density is lower than $\sim 10^5 \text{ cm}^{-3}$. The broad emission lines are absent in objects classified as “pure” type II AGN (except for a weak scattered component visible in polarized light). Less obscured AGN are classified as type 1.9 and type 1.8 and show broad components in, respectively, the $\text{H}\alpha$ line and both the $\text{H}\alpha$ and $\text{H}\beta$ lines. The optical spectrum of the prototype Seyfert 2 NGC 1068 is shown in Figure 6.10.

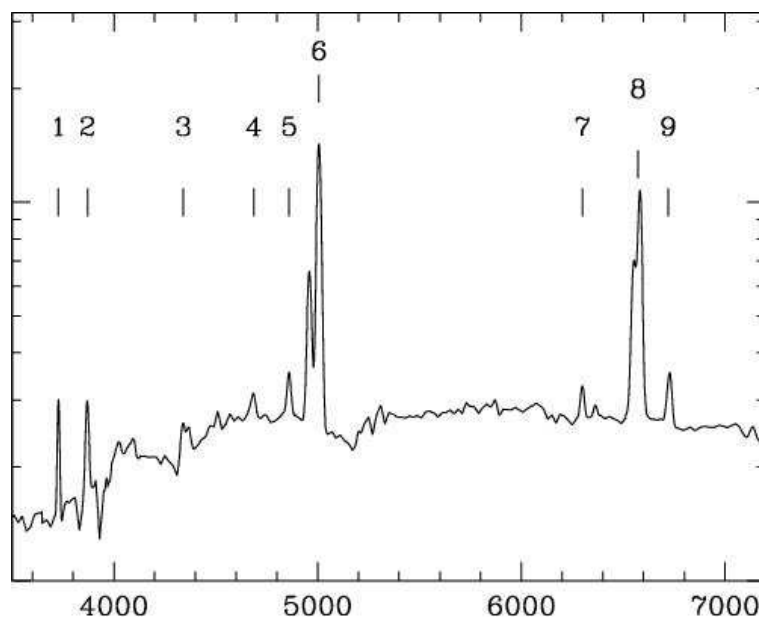


Figure 6.10. Optical spectrum of the prototype Seyfert 2 galaxy NGC 1068. Main emission lines are 1: [OII]λ3727Å, 2: [NeII]λ3869Å, 3: Hγ, 4: HeII λ4687Å, 5: Hβ, 6: [OIII]λ5007Å, 7: [OI]λ6300Å, 8: Hα+[NII]λ6585Å, 9: [SII]λ6732Å.

In heavily obscured AGN, when only emission lines are seen, it can be hard to distinguish an AGN from a starburst (this will be discussed in §6.4). A major indicator of the presence of an AGN is the high ratio of high ionization lines, such as [OIII]λ5007 Å or N V, with respect to low ionization lines, such as Hβ or Hα. These narrow emission lines are the result of the reprocessing of nuclear radiation by gas not covered by the nuclear absorber because it lies outside the obscuring region. The central

emission (continuum and broad lines) can be scattered by circumnuclear hot gas, or by dust from some region outside of the obscuring region that lies in a direction with a clear view of the central source. This component is typically too weak with respect to the galaxy emission to be seen in the total spectrum, but it clearly emerges in polarimetric observations. The implication is that the obscuring region has a flattened distribution.

Historically, the observation of broad lines in the polarized spectrum of NGC 1068 was fundamental for the formulation of the unified model of AGN, which states that type I and type II AGN are intrinsically the same objects and differ only in the orientation of the circumnuclear absorber (Antonucci & Miller 1985).

6.3.3 X-rays

Obscuration in the X-rays is due to photoelectric absorption (dominant below ~ 3 keV) and Compton scattering (dominant from ~ 7 to ~ 30 keV). The X-ray spectral properties of obscured AGN depend on the amount of absorbing column density: column densities below $\sim 1.5 \times 10^{24} \text{ cm}^{-2}$ produce a photoelectric cut-off at energies between 1 and 10 keV (in this case, the source is “Compton thin”); column densities between $\sim 10^{24} \text{ cm}^{-2}$ and $\sim 10^{25} \text{ cm}^{-2}$ absorb the X-ray primary emission up to several tens of keV; even higher column densities completely obscure the central source in the X-rays.

In heavily absorbed sources (“Compton thick”, $N_H > 10^{24} \text{ cm}^{-2}$), the two main spectral features are a prominent iron $K\alpha$ emission line with $EW \sim 1 - 3$ keV, and a reflected and/or scattered continuum. In less obscured sources, the EW of the iron line depends on the fraction of the intrinsic continuum emission absorbed at the line energy; for $N_H < 10^{23} \text{ cm}^{-2}$, values typical of type I AGN are observed ($EW \sim 100 - 300$ eV), in agreement with the unified model. The reflected/scattered component is the same as described in §6.2.4 for type I AGN.

In Figure 6.11, we plot the 1 – 100 keV spectra of four representative obscured AGN: MCG-5-23-16 ($N_H = 10^{22} \text{ cm}^{-2}$, Risaliti 2002), NGC 4388 ($N_H = 4 \times 10^{23} \text{ cm}^{-2}$, Risaliti 2002), NGC 4945 ($N_H = 2 \times 10^{24} \text{ cm}^{-2}$, Vignati et al. 1999), and NGC 1068 ($N_H > 10^{25} \text{ cm}^{-2}$, Matt et al. 1999).

6.3.4 Relation between Dust and Gas Absorption

According to the standard paradigm of the unified model, X-ray absorption should be observed in optically type II objects. This is indeed

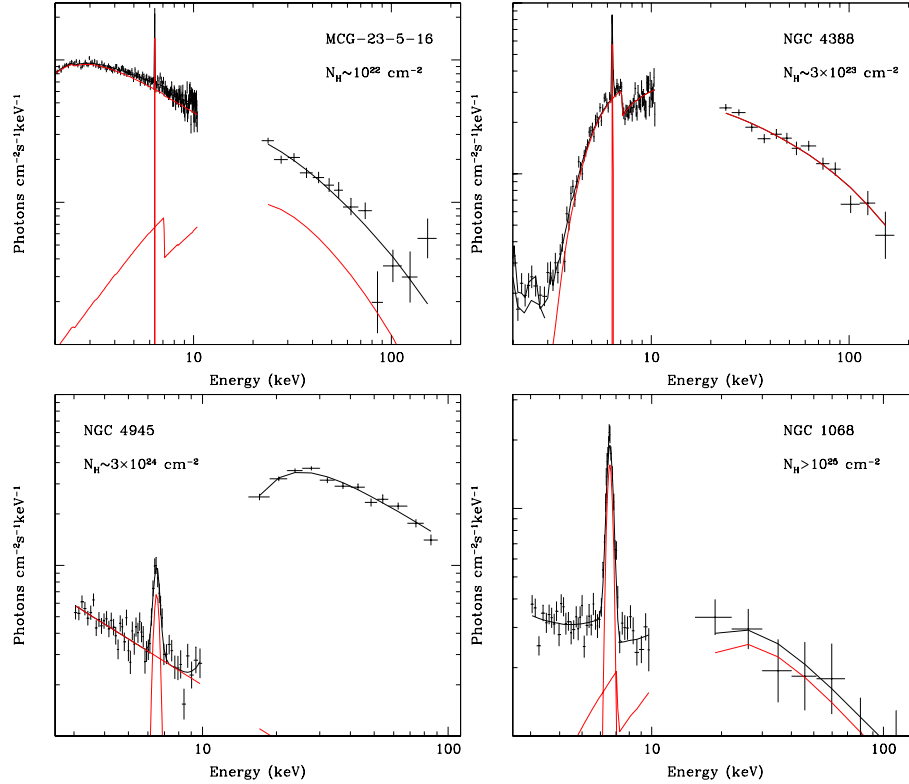


Figure 6.11. Four 2–100 keV *BeppoSAX* best fit X-ray spectra of Seyfert 2 galaxies. Main components of the best fit models are also shown. MCG-5-23-16 and NGC 4388 (Risaliti 2002) are “Compton thin”, i.e., they are dominated by the primary emission down to a few keV. In MCG-5-23-16, a cold reflection component also gives a measurable contribution. The continuum in the Compton-thick source NGC 4945 (Guainazzi et al. 2000) is due to a warm reflection component in the 2–10 keV range, while at higher energies the intrinsic component emerges. Note the high ratio between the 10–100 keV and the 2–10 keV emission, as compared with the Compton-thin sources. NGC 1068, also Compton-thick (Matt et al. 1999), shows a cold reflection and a warm reflection component. Equivalent widths of the iron line are ~ 100 eV in MCG-5-23-16, ~ 500 eV in NGC 4388, and 1–2 keV in NGC 4945 and NGC 1068.

what has been found in many local AGN. However, recent observations challenge this simple view and suggest a more complex scenario.

A direct measurement of the dust-to-gas ratio is possible in objects with intermediate optical classification, i.e., Seyfert 1.8 or 1.9. These show clear signs of absorption in the optical/near-IR but still have broad components in some of the brightest emission lines. In these cases, an estimate of the dust absorption can be obtained from the ratio of the

emission line fluxes (typically, the hydrogen lines) and can be compared with the absorbing column density measured in the X-rays.

For a Galactic dust composition and dust-to-gas ratio, the relation between optical extinction and X-ray absorption is $A_V \sim 4.5 \times 10^{-21} N_H$. Therefore, one would expect objects with optical broad lines to have X-ray column densities not higher than 10^{22} cm^{-2} . Maccacaro, Perola, & Elvis (1982) and Maiolino et al. (2001) analyzed a sample of bright, intermediate Seyferts and found that X-ray absorption is systematically higher than expected from optical extinction by a factor of ~ 10 . The physical explanation of this result may be a lower than Galactic dust-to-gas ratio, or a different composition of dust grains. The observed SEDs of these objects can be significantly different than standard type I and type II templates, with lower UV, larger IR, and heavily absorbed X-rays (Ward et al. 1982).

Moving to more extreme cases, BAL quasars are objects with no or little dust extinction in the optical/UV, but with broad, blueshifted, and often saturated absorption lines. Many of them also only have extremely faint X-ray emission (note, however, that there are exceptions, such as the BAL quasars found in deep X-ray surveys; Barger et al. 2002).

There is now convincing evidence that these objects are intrinsically normal quasars, covered by a high column density of dust-free gas that is responsible for heavy absorption in the X-rays and absorption lines in the optical/UV. A strong correlation between these two absorption features has been found by Brandt et al. (2001), and recent X-ray observations are starting to directly measure the X-ray column densities of these objects. A clear example is the *BeppoSAX* observation of the X-ray weak BAL quasar MKN 231, which revealed powerful hard X-ray emission above 10 keV obscured by a column density $N_H > 10^{24} \text{ cm}^{-2}$ (Braitto et al. 2004, see Fig. 6.12).

Other examples of objects with strongly differing optical and X-ray absorption are found in quasar surveys where selection criteria other than optical/UV color are used. An interesting example is the sample of “red” quasars discovered with the 2MASS near-IR survey (Cutri et al. 2001). The selection criterion adopted in this case is $J - K > 2$, which is efficient at low redshifts where the minimum in the quasar emission, due to the sublimation temperature of dust, is observed in the J band. *Chandra* observations of a sample of these “red”, yet broad-line objects (Wilkes et al. 2002), revealed that they are extremely faint in the X-rays, probably due to absorption by a column density of order 10^{23} cm^{-2} .

Another case of X-ray weakness in optically type I quasars is found in the sample of quasars from the Hamburg survey (Hagen et al. 2001) which also have *ROSAT* observations (Risaliti et al. 2001). Most of

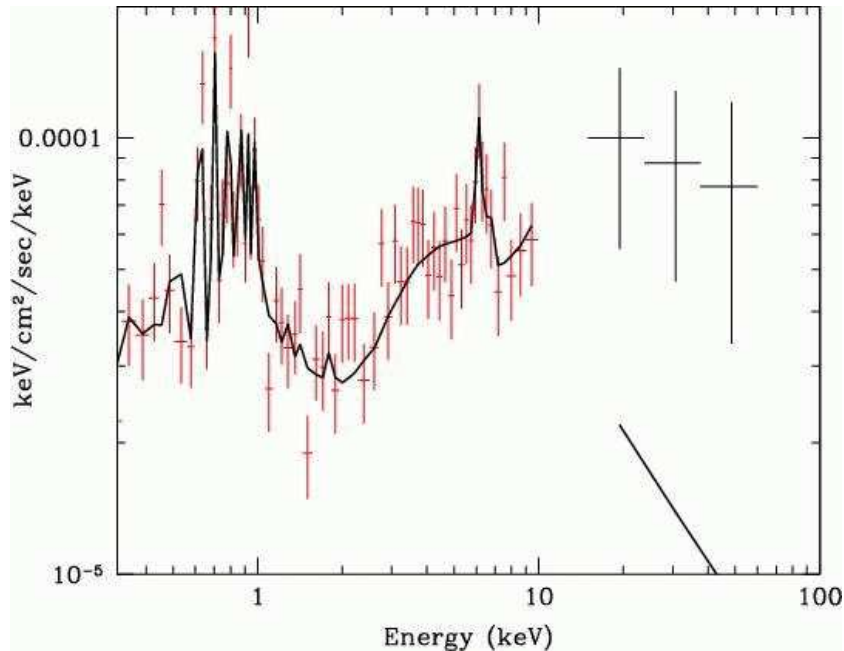


Figure 6.12. *XMM-Newton* and *BeppoSAX* spectrum of MKN 231. Figure obtained using data and model of Braito et al. (2004). Model shown here is a best fit to the 0.5 – 10 keV emission. The large excess at $E > 10$ keV is due to the intrinsic emission of the AGN, which is absorbed by a column density $N_H \sim 2 \times 10^{24} \text{ cm}^{-2}$.

these objects, which are slightly redder in the optical than standard blue quasars (the selection criterion was based both on blue color and on low resolution spectroscopy), are undetected by *ROSAT*, contrary to what was expected assuming a “normal” α_{OX} . Subsequent *Chandra* observations of a subsample of these objects revealed that they are underluminous in the X-rays by a factor of ~ 3 to ~ 100 with respect to PG quasars (Risaliti et al. 2003a). It is not clear whether the observed X-ray weakness is an intrinsic property of these objects (as most of the *Chandra* spectra seem to suggest) or whether it is due to absorption. In any case, they are part of a population of quasars with SEDs different than that of standard type I or type II AGN.

In addition to the cases described above of optically type I AGN with the X-ray properties of type II AGN, several examples are known of the opposite case, i.e., objects with type II optical properties and no hint of absorption in the X-rays. Panessa et al. (2003) described a sample of

local sources optically classified as Seyfert 2 galaxies with no measured X-ray absorbing column density in excess of the Galactic value.

6.4 Finding Obscured AGN in the Universe

In the previous two sections, we described the main properties of AGN continua for both obscured and unobscured sources, while neglecting the problem of disentangling the AGN emission from that of the host galaxy. Type I AGN are easily detected in the optical down to luminosities that are intrinsically weaker than the total host galaxy emission. In this case, high signal-to-noise and careful galaxy subtraction can detect the central AGN emission (Ho, Filippenko, & Sargent 1999). Type II AGN, however, can be extremely elusive, even when they dominate the bolometric emission of the galaxy, since most of their primary emission is thermally reradiated into the IR. Since the IR is simply a sum of blackbodies, to a good approximation all signatures of the origin of the luminosity are lost. Hence it is extremely difficult to distinguish an AGN contribution from that of star-forming regions. This problem is particularly important in the study of high luminosity sources, such as the Ultraluminous Infrared Galaxies (ULIRGs; Sanders & Mirabel 1996) and their probable high redshift analogs, the powerful submillimeter emitters detected in SCUBA surveys (e.g., Smail, Ivison, & Blain 1997; Barger et al. 1998; Hughes et al. 1998). Distinguishing AGN contributions from star formation is of great importance in determining which class of source makes up the submillimeter/IR background, and therefore in knowing the relative contributions that accretion onto supermassive black holes and star formation make to the total luminosity of the universe.

6.4.1 Indicators for (Local) AGN and Starbursts

We next discuss the main indicators of optically obscured AGN (hereafter, we use “obscured” to mean that the optical/UV continuum and broad emission line spectrum is not observable) in each wavelength band, and the limits of each technique. Then we try to draw some general conclusions on the possibility of detecting AGN activity in galaxies, now and in the foreseeable future. Two main elements are relevant for the effectiveness of the different indicators: (1) the amount of X-ray absorbing column density N_H and optical extinction A_V , and (2) the fraction of solid angle covered by the obscuring medium.

- *X-rays*. If the X-ray absorbing column density is not larger than 10^{25} cm^{-2} , the direct $> 10 \text{ keV}$ X-ray emission of the AGN can penetrate the absorber. In this case, the hard X-ray emission will be at least an order of magnitude higher than that of the host galaxy, down to

luminosities $\sim 10^{41}$ ergs s $^{-1}$. With arcsecond (*Chandra*) resolution, the contrast is improved by a factor of 10–100 for $z \leq 0.1$, though *Chandra*'s effective upper energy bound of ~ 7 keV limits the detection to $N_H < 10^{23}$ cm $^{-2}$ (this limit moves up to 10^{24} cm $^{-2}$ for objects at redshifts $z \sim 1$). In these cases, the detection of the AGN is unambiguous.

The contribution of the host galaxy to the hard X-ray emission is usually modeled by two components: the thermal emission due to warm interstellar gas (kT ~ 0.1 -1 keV), and the contribution from compact sources (dominated by X-ray binaries) that, on average, is reproduced by a power law with $\alpha \sim -0.5$ to -0.7 , or by a thermal component with kT ~ 20 keV (Fabbiano 1989). The luminosity of these components can be of the same order as—or greater than—that of the obscured AGN ($L_X < 10^{40}$ ergs s $^{-1}$ for spirals; $L_X \sim 10^{41}$ ergs s $^{-1}$ for ellipticals and starbursts). From the observed direct X-ray emission, it is possible to give a rough estimate to the bolometric emission of the AGN using the information of the average SED discussed in §6.2. Examples of the effectiveness of hard X-ray observations include ULIRG MKN 231, shown in Figure 6.12 (discussed in §6.3.4 as a BAL quasar), and NGC 6240, an ULIRG with no evidence of AGN activity below 20 – 30 keV (except, perhaps, for some indication from mid-IR coronal lines, Lutz et al. 2003). A *BeppoSAX* observation of NGC 6240 discovered a powerful AGN with a column density $N_H > 10^{24}$ cm $^{-2}$ that showed up at energies $E > 20$ keV (Vignati et al. 1999).

However, despite these impressive examples, this method has so far proved to be useful only in a few cases. A *BeppoSAX* search for ULIRGs known to host an AGN from other indicators (described below) in the 10 – 100 keV band failed to detect the nuclear activity in most cases (Risaliti et al. 2004, in preparation). This implies that most of these sources are obscured by column densities $N_H > 10^{25}$ cm $^{-2}$.

If $N_H > 10^{25}$ cm $^{-2}$, no direct emission can penetrate the obscuring medium because multiple Compton scatterings gradually remove energy from the photons until they can be photoelectrically absorbed. In this case, the only way to detect the AGN is through reflected (scattered) emission. The main spectral properties of a cold reflection dominated AGN are a flat spectrum ($\alpha > -1$ in the 2 – 10 keV band) and a prominent iron line (EW >1 keV) at ~ 6.4 keV. In principle, two methods can be used to disentangle the two contributions, based on spatial and spectral analyses, respectively.

1) High spatial resolution can help to resolve the nuclear region where the AGN emission is dominant. This approach is obviously most useful when used on nearby sources. A case study, which shows both the

power and the limitations of this approach, is the *Chandra* observation of the ULIRG Arp 220. The subarcsecond resolution instruments of *Chandra* resolved a weak point-like hard X-ray source with luminosity $\sim 4 \times 10^{40}$ ergs s^{-1} (Clements et al. 2003), which is probably associated with an AGN. No previous spectral analysis was able to disentangle this component from the diffuse X-ray emission because of the orders of magnitude worse spatial resolution. However, even in the Arp 220 case, we cannot rule out that the observed hard emission is due to $\sim 10 - 100$ X-ray binaries in a region of intense star formation (the size limit for a *Chandra* point source at the redshift of Arp 220, $z = 0.018$, is ~ 400 pc).

2) Spectral decomposition of the AGN and starburst components requires high effective area. Recently, an *XMM-Newton* survey of nearby, bright ULIRGs provided the best X-ray spectra of ULIRGs (Franceschini et al. 2003). The AGN component was clearly detected in 3 out of 8 sources through the high EW 6.4 keV iron line and the flat continuum. However, in the remaining five sources, the case is ambiguous, as the presence of a completely obscured ($N_H > 10^{24}$ cm^{-2}) AGN cannot be ruled out.

- *Optical/UV.* By definition, optically obscured (type II) AGN do not show any intrinsic continuum emission in the optical/UV band. The two main ways to search for AGN in these wavebands are through scattered (polarized) light and narrow emission line ratios. Both require that there are some unobscured directions out of the nucleus.

Scattering by warm electrons has been briefly discussed in §6.3. In the polarized spectrum, broad emission lines can be detected, unambiguously revealing a central AGN.

The main method for classifying narrow emission line objects is through the ratio of emission line fluxes: high ionization lines are expected to be stronger in AGN than in starbursts. The main optical emission lines shown in Figure 6.10, and listed in the caption, are roughly the same as in a spectrum of a starburst galaxy. In Figure 6.13, we show a classical diagnostic diagram, first introduced by Veilleux & Osterbrock (1987), in which type II AGN are clearly separated from starbursts. In the same figure, a third class of objects is shown, the so-called LINERs (Low Ionization Emission Line Objects). The origin of their emission (nuclear activity or star formation) is not yet clear.

- *Infrared.* A general indicator of AGN activity is a warm IR spectrum. The IRAS 25 – 60 μm color is rather effective in finding AGN-powered IR sources (see, for example, de Grijp et al. 1997). However,

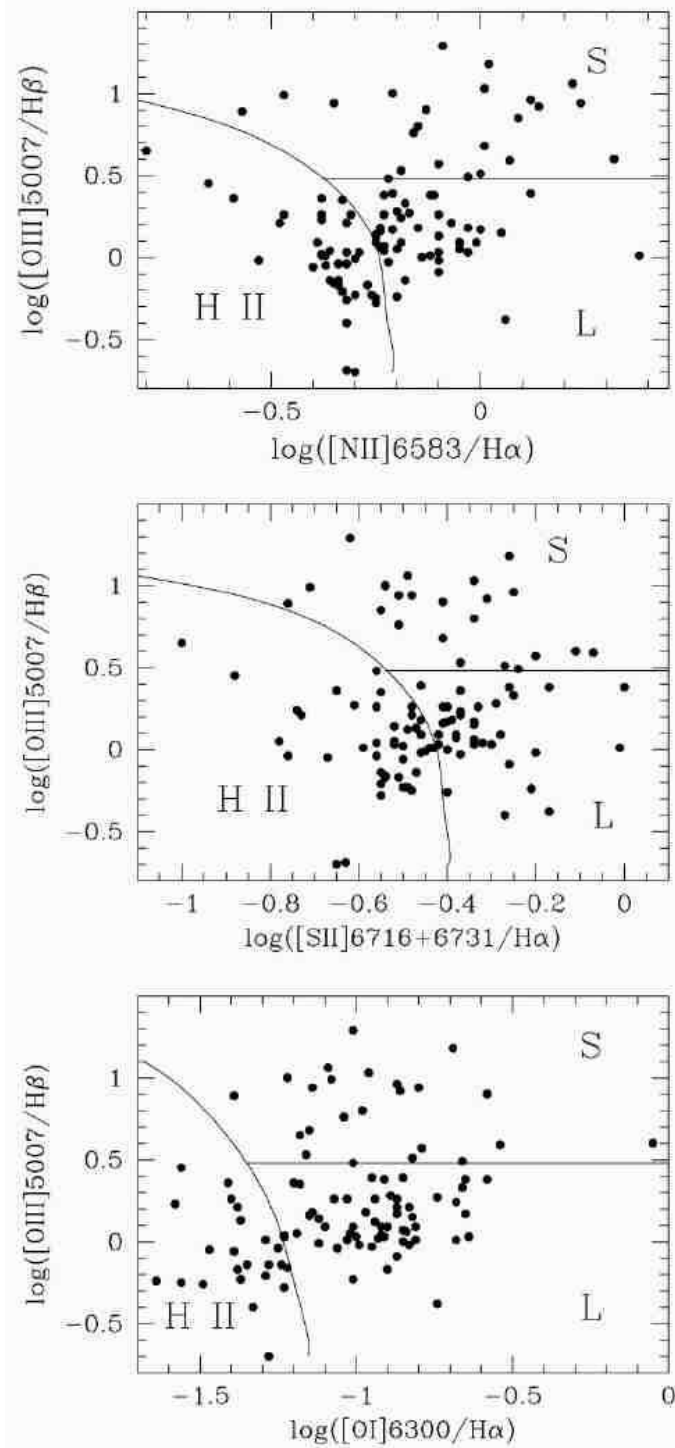


Figure 6.13. Diagnostic diagrams based on narrow emission line ratios for a sample of bright ultraluminous infrared galaxies. Figure from Veilleux, Kim, & Sanders (1999; their Fig. 2).

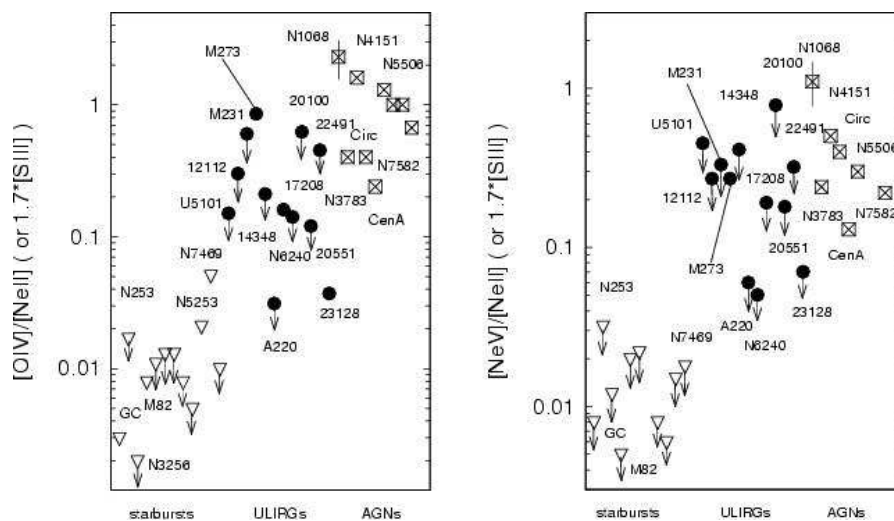


Figure 6.14. Diagnostic diagrams based on mid-IR emission lines. Inverted triangles and squares denote sources optically classified as starbursts and AGN, respectively. Circles denote ULIRGs. Figure from Genzel et al. (1998; their Fig. 3).

while a high $25 - 60\mu\text{m}$ color can be considered an indicator of AGN activity, independent confirmation is needed.

ISO has enhanced the analytic capability of IR analysis. For example, Laurent et al. (2000) have shown that the ratio between the $12 - 18\mu\text{m}$ and the $5 - 8.5\mu\text{m}$ emission (these are the ranges of two filters in the ISOPHOT instrument on the *ISO* satellite) is effective in discriminating the AGN and starburst contributions at redshifts between 0.4 and 1. At a finer level of detail, when low resolution spectroscopy is available, broad emission features in the mid-IR band can be used as effective AGN indicators. For example, the absence of a broad $7.7\mu\text{m}$ emission, due to Polycyclic Aromatic Hydrocarbon (PAH) molecules, is believed to be an indicator of AGN emission, both because of the strength of this indicator in control samples and for physical considerations: PAH molecules should be destroyed by the high energy continuum of an AGN.

Finally, higher resolution *ISO* SWS spectra provide useful indicators of the relative AGN/starburst contributions. As in the case of optical lines, high excitation emission lines are tracers of AGN activity, while strong, low excitation lines are a sign of starbursting activity. For example, $[\text{O IV}]\lambda 25.9\mu\text{m}$ and $[\text{Ne V}]\lambda 14.3\mu\text{m}$ are among the strongest high excitation mid-IR emission lines, while $[\text{Ne II}]\lambda 12.9\mu\text{m}$ and $[\text{S III}]\lambda 18.7\mu\text{m}$ are strong low excitation lines. An example of the use of these indi-

cators can be found in Genzel et al. (1998), where the $[\text{O IV}]/[\text{Ne II}]$ and $[\text{Ne V}]/[\text{Ne II}]$ ratios of a sample of nearby, bright ULIRGs are compared with those of comparison samples of local AGN and starbursts (see Fig. 6.14). The power of this diagnostic is also well illustrated by its application to the *ISO* spectrum of the galaxy NGC 6240. This source, as discussed above, is known from hard X-ray (10–100 keV) observations to host a powerful AGN, but it does not reveal any indication of an AGN at longer wavelengths, except for a strong $[\text{O IV}]\lambda 25.9\mu\text{m}$ in the *ISO* SWS spectrum (Lutz et al. 2003). All the IR methods discussed above will be much more effective, and applicable at higher redshift and/or fainter objects, with the new observations of the *Spitzer Space Telescope*.

Moving to shorter wavelengths, recent observations in the *L*-band from ground-based telescopes have provided interesting new ways to disentangle AGN and starburst activity: the $3.3\mu\text{m}$ PAH emission feature is a starburst indicator (Tokunaga et al. 1991), AGN are characterized by an absorption feature at $\sim 3.4\mu\text{m}$ due to hydrocarbon dust grains (Pendleton et al. 1994), and the $3 - 4\mu\text{m}$ continuum is much steeper in AGN-dominated sources. As examples, we plot in Figure 6.15 a starburst spectrum (NGC 253, Imanishi & Dudley 2000) and an AGN spectrum (IRAS 19254+7245, Risaliti et al. 2003c).

- *Radio*. High spatial resolution radio observations can provide useful indicators of AGN activity. Very Long Baseline Interferometry (VLBI) observations of ULIRGs (Lonsdale et al. 1993; Smith et al. 1998) showed that compact, high brightness temperature (well above starburst temperatures; $T_b > 10^5$ K) sources are preferentially found in objects classified optically as AGN. Physically, compact and high luminosity radio emission can only be explained by AGN activity, or by assuming the simultaneous presence of several extremely luminous radio supernovae in regions with a radius of less than 1 kpc, a highly unlikely event, even in the most intense starburst regions.

Recently, a radio VLA survey of the ULIRGs in the IRAS 1 Jy sample (Kim & Sanders 1998) showed that compact radio emission is present in most LINER classified ULIRGs, similar to that found in objects optically classified as AGN, and contrary to what is found in starburst galaxies (Nagar et al. 2003). This result is particularly interesting since it provides a method to estimate the AGN incidence in a class of objects—LINERs—for which optical spectroscopic criteria do not give clear indications (as shown in Fig. 6.13).

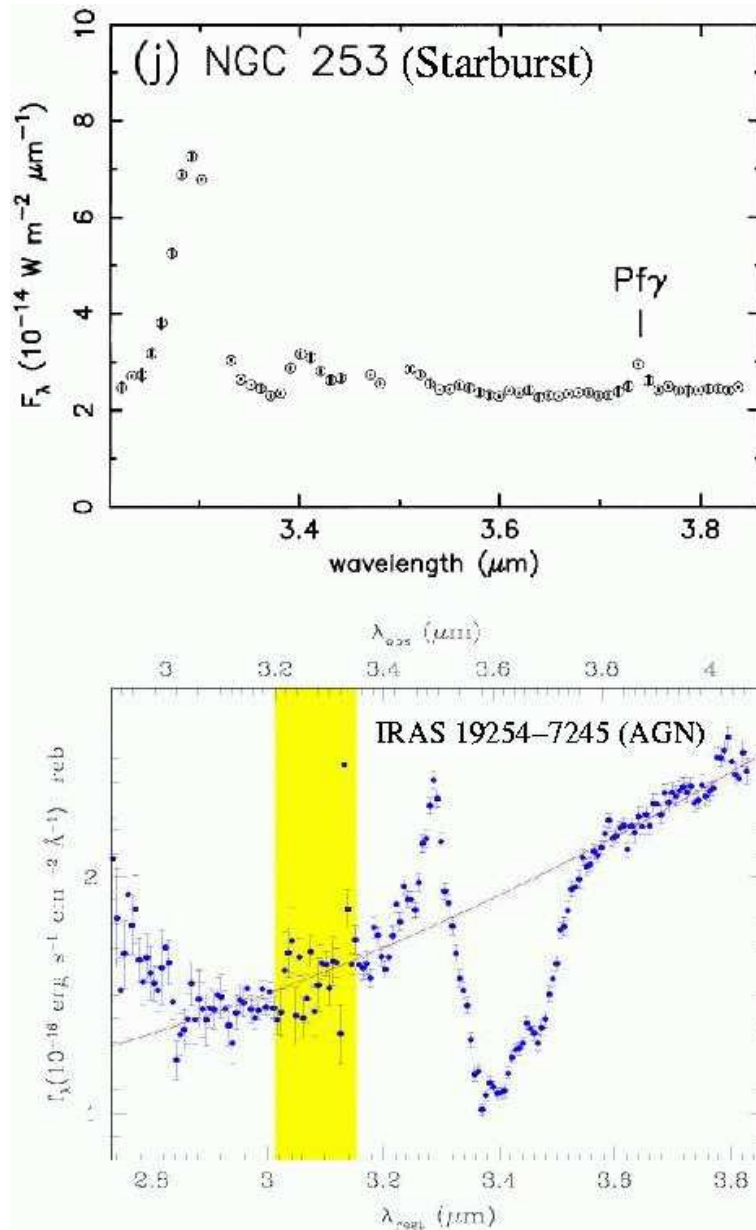


Figure 6.15. *L*-band spectrum of the starburst galaxy NGC 253 (from Imanishi & Dudley 2000; their Fig. 2j) and of the AGN-dominated ULIRG IRAS 19254+7245 (Risaliti et al. 2003c; their Fig. 1). The most evident features are the $3.3\mu\text{m}$ PAH emission line in both spectra and the $3.4\mu\text{m}$ absorption feature in IRAS 19254+7245. Shaded band in the spectrum of IRAS 19254+7245 indicates a wavelength interval with low atmospheric transmission.

6.4.2 Limitations

At present, the methods described above can be applied only to bright and local AGN (with a few exceptions, like the hard X-ray diagnostics, and the ISOPHOT colors). Indeed, almost all of the examples shown here are about observations of nearby, powerful IR galaxies. These sources are not only interesting in themselves but represent analogs of the population dominating the submillimeter background, which probably comprises high redshift galaxies. Understanding the energy source of these populations would ultimately give us the ability to estimate the total fraction of the radiated energy of the universe due to AGN. It is therefore very important to understand the perspective of extending these methods to fainter and more distant sources.

There are two main limitations of the methods described above, one due to physical limits, and one due to observational capabilities. Observations of better quality can be done with forthcoming instruments and can extend these diagnostics to a much wider range of sources. However, all the methods described above are based on the detection of either direct AGN emission or scattered, reflected, or reprocessed (in the case of emission lines) emission. If the gas column density is higher than $\sim 10^{25} \text{ cm}^{-2}$, the dust extinction is higher than $\sim 8 - 10$ magnitudes (even in the IR), and the obscuration of the source is complete along all lines-of-sight, then none of the above methods can be used. Even the mid-IR emission will be self-absorbed and reprocessed at longer wavelengths, so no big differences are expected in the far-IR spectra of AGN and starburst dominated sources. In this extreme case, all the observed emission of the active nucleus will be thermally reprocessed by the circumnuclear obscurer. There is then only one method to search for AGN in these sources: spatial resolution. In principle, high spatial resolution is rather simple: if high far-IR emission is detected in too small of a region, so that even the most compact starburst can be ruled out, then only an AGN can be the energy source. In order to be effective, this requires resolutions of at most a few tens of parsecs for ULIRGs, which is far from being reached for the nearest ULIRGS, even with the new *Spitzer Space Telescope*. (One milliarcsec at $z = 0.05$ corresponds to $\sim 1 \text{ pc}$ with $H_0 = 70 \text{ km s}^{-1} \text{ Mpc}^{-1}$). However, this remains a possibility (maybe the only one) for a future solution to this problem.

In summary, will we ever be able to understand the origin of the emission in the powerful far-IR and submillimeter sources and to estimate the total contribution of accretion to the energy output of the universe? The answer depends both on the improvement of instrumentation (and here no limit can be put on the development of science and technology)

and on nature—even the most powerful and compact emission in the universe can be completely hidden by a thick enough screen.

6.5 Summary

We have reviewed the main spectral properties of quasars, with an emphasis on continuum emission and a brief treatment of the main emission and absorption features.

In the first part, we built an updated SED of quasars, mainly based on continuum emission of local ($z < 0.4$) PG quasars. The main improvements with respect to the previous reference work in the field, the atlas of Elvis et al. (1994), are: 1) the treatment of selection effects in the X-rays, which allowed us to estimate the correct optical-to-X-ray flux ratio for local quasars, 2) the extension of the SED in the UV at wavelengths shortward of the Lyman break, using *HST* observations of quasars, 3) the inclusion of the new IR data obtained with *ISO*, and 4) the use of a larger sample in the computation of the average spectral properties of quasars.

In the second part, we reviewed the main spectral properties of obscured quasars. We also discussed the relation between dust and gas absorption, briefly describing the cases of X-ray obscured objects with no or little optical/near-IR absorption.

In the third and final part, we summarized the methods for finding obscured AGN in the universe, focusing on the problem of disentangling the active nucleus component in infrared luminous sources and discussing the still open problems. Despite the improvements of the last few years, what we know is most likely only a fraction of the obscured quasars present in the universe.

Acknowledgments

We wish to thank Amy Barger for giving us the opportunity to contribute to this book, and for her really infinite patience with our very long delays in preparing the manuscript.

References

- Antonucci, R. R. J., & Miller, J. S. 1985, *ApJ*, 297, 621
- Avni, Y., & Tananbaum, H. 1982, *ApJL*, 262, L17
- Avni, Y., & Tananbaum, H. 1986, *ApJ*, 305, 83
- Bechtold, J., et al. 2003, *ApJ*, 588, 119
- Baldwin, J. A. 1977, *ApJ*, 214, 679
- Barger, A. J., Cowie, L. L., Sanders, D. B., Fulton, E., Taniguchi, Y., Sato, Y., Kawara, K. & Okuda, H. 1998, *Nature*, 394, 248

- Barger, A. J., Cowie, L. L., Brandt, W. N., Capak, P., Garmire, G. P., Hornschemeier, A. E., Steffen, A. T., & Wehner, E. H. 2002, *AJ*, 124, 1839
- Barger, A. J., et al. 2003, *AJ*, 126, 632
- Braitto, V., et al. 2004, *MNRAS*, in press
- Brandt, W. N., Laor, A., & Wills, B. J. 2000, *ApJ*, 528, 637
- Brotherton, M. S., Tran, H. D., Becker, R. H., Gregg, M. D., Laurent-Muehleisen, S. A., & White, R. L. 2001, *ApJ*, 546, 775
- Brusa, M., et al. 2003, *A&A*, 409, 65
- Chini, R., Kreysa, E., & Biermann, P. L. 1989, *A&A*, 219, 87
- Clements, D. L., McDowell, J. C., Shaked, S., Baker, A. C., Borne, K., Colina, L., Lamb, S. A., & Mundell, C. 2002, *ApJ*, 581, 974
- Crenshaw, D. M., Kraemer, S. B., Boggess, A., Maran, S. P., Mushotzky, R. F., & Wu, C. 1999, *ApJ*, 516, 750
- Croom, S. M., et al. 2002, *MNRAS*, 337, 275
- Cutri, R., et al. 2001, in “The New Era of Wide Field Astronomy”, Eds. R. Clowes, A. Adamson, & G. Bromage (San Francisco: ASP Conference Series), 232, p78
- Czerny, B., & Elvis, M. 1987, *ApJ*, 321, 305
- de Grijp, M. H. K., Lub, J., & Miley, G. K. 1987, *A&AS*, 70, 95
- Elitzur, M., Nenkova, M., & Ivezić, Z., 2004, in “The Neutral ISM in Starburst Galaxies”, in press (astro-ph/0309040)
- Elvis, M. 1985, in “Galactic and Extra-Galactic Compact X-ray Sources”, Eds. Y. Tanaka & W. H. G. Lewin, p291
- Elvis, M., Maccacaro, T., Wilson, A. S., Ward, M. J., Penston, M. V., Fosbury, R. A. E., & Perola, G. C. 1978, *MNRAS*, 183, 129
- Elvis, M., Risaliti, G., & Zamorani, G. 2002, *ApJ*, 565, L75
- Elvis, M., et al. 1994, *ApJS*, 95, 1 (E94)
- Fabbiano, G. 1989, *ARA&A*, 27, 87
- Fabian, A. C., & Iwasawa, K. 1999, *MNRAS*, 303, L
- Fabian, A. C., Rees, M. J., Stella, L., & White, N. E. 1989, *MNRAS*, 238, 729
- Fabian, A. C., et al. 2002, *MNRAS*, 335, L1
- Franceschini, A., et al. 2003, *MNRAS*, 343, 1181
- Francis, P. J., Hewett, P. C., Foltz, C. B., Chaffee, F. H., Weymann, R. J., & Morris, S. L. 1991, *ApJ*, 373, 465
- Genzel, R., et al. 1998, *ApJ*, 498, 579
- George, I. M., Turner, T. J., Netzer, H., Nandra, K., Mushotzky, R. F., & Yaqoob, T. 1998, *ApJS*, 114, 73
- George, I. M., Turner, T. J., Yaqoob, T., Netzer, H., Laor, A., Mushotzky, R. F., Nandra, K., & Takahashi, T. 2000, *ApJ*, 531, 52
- Ghisellini, G., Haardt, F., & Matt, G. 1994, *MNRAS*, 267, 743

Gilli, R., Salvati, M., & Hasinger, G. 2001, *A&A*, 366, 407
Guainazzi, M., Matt, G., Brandt, W. N., Antonelli, L. A., Barr, P., & Bassani, L. 2000, *A&A*, 356, 463
Haas, M., et al. 2003, *A&A*, 402, 87
Hagen, H.-J., Groote, D., Engels, D., & Reimers, D. 1995, *A&AS*, 111, 195
Hughes, D. H., et al. 1998, *Nature*, 394, 241
Imanishi, M., & Dudley, C. C. 2000, *ApJ*, 545, 701
Kellermann, K. I., Sramek, R., Schmidt, M., Shaffer, D. B., & Green, R. 1989, *AJ*, 98, 1195
Kim, D.-C., & Sanders, D. B. 1998, *ApJS*, 119, 41
Krongold, Y., Nicastro, F., Brickhouse, N. S., Elvis, M., Liedahl, D. A., & Mathur, S. 2003, *ApJ*, 597, 832
Kuraszkiewicz, J. K., et al. 2003, *ApJ*, 590, 128
Laor, A. 1991, *ApJ*, 376, 90
Laor, A., Fiore, F., Elvis, M., Wilkes, B. J., & McDowell, J. C. 1997, *ApJ*, 477, 93
Laurent, O., Mirabel, I. F., Charmandaris, V., Gallais, P., Madden, S. C., Sauvage, M., Vigroux, L., & Cesarsky, C. 2000, *A&A*, 359, 887
Lonsdale, C. J., Smith, H. J., & Lonsdale, C. J. 1993, *ApJ*, 405, L9
Lutz, D., Sturm, E., Genzel, R., Spoon, H. W. W., Moorwood, A. F. M., Netzer, H., & Sternberg, A. 2003, *A&A*, 409, 867
Maccacaro, T., Perola, G. C., & Elvis, M. 1982, *ApJ*, 257, 47
Maiolino, R., Marconi, A., Salvati, M., Risaliti, G., Severgnini, P., Oliva, E., La Franca, F., & Vanzani, L. 2001, *A&A*, 365, 28
Maiolino, R., & Rieke, G. H. 1995, *ApJ*, 454, 95
Malkan, M. A., & Sargent, W. L. W. 1982, *ApJ*, 254, 22
Matt, G., et al. 1997, *A&A*, 325, L13
Mineo, T., et al. 2000, *A&A*, 359, 471
Nagar, N. M., Falcke, H., Wilson, A. S., & Ho, L. C. 2000, *ApJ*, 542, 186
Nagar, N. M., Wilson, A. S., Falcke, H., Veilleux, S., & Maiolino, R. 2003, *A&A*, 409, 115
Nandra, K., George, I. M., Mushotzky, R. F., Turner, T. J., & Yaqoob, T. 1997, *ApJ*, 477, 602
Neufeld, D. A., Maloney, P. R., & Conger, S. 1994, *ApJ*, 436, L127
Panessa, F., & Bassani, L. 2002, *A&A*, 394, 435
Pendleton, Y. J., Sandford, S. A., Allamandola, L. J., Tielens, A. G. G. M., & Sellgren, K. 1994, *ApJ*, 437, 683
Perola, G. C., Matt, G., Cappi, M., Fiore, F., Guainazzi, M., Maraschi, L., Petrucci, P. O., & Piro, L. 2002, *A&A*, 389, 802
Risaliti, G. 2002, *A&A*, 386, 379
Risaliti, G., Elvis, M., Gilli, R., & Salvati, M. 2003a, *ApJ*, 587, L9

- Risaliti, G., Gilli, R., Maiolino, R., & Salvati, M. 2000, *A&A*, 357, 13
- Risaliti, G., Marconi, A., Maiolino, R., Salvati, M., & Severgnini, P. 2001, *A&A*, 371, 37
- Risaliti, G., Woltjer, L., & Salvati, M. 2003b, *A&A*, 401, 895
- Risaliti, G., et al. 2003c, *ApJ*, 595, L17
- Sanders, D. B., & Mirabel, I. F. 1996, *ARA&A*, 34, 749
- Sanders, D. B., Phinney, E. S., Neugebauer, G., Soifer, B. T., & Matthews, K. 1989, *ApJ*, 347, 29
- Schmidt, M., & Green, R. F. 1983, *ApJ*, 269, 352
- Schneider, D. P., Schmidt, M., & Gunn, J. E. 1994, *AJ*, 107, 1245
- Shields, G. A. 1978, *Nature*, 272, 706
- Smail, I., Ivison, R. J., & Blain, A. W. 1997, 490, L5
- Smith, H. E., Lonsdale, C. J., & Lonsdale, C. J. 1998, *ApJ*, 492, 137
- Tanaka, Y., et al. 1995, *Nature*, 375, 659
- Telfer, R. C., Zheng, W., Kriss, G. A., & Davidsen, A. F. 2002, *ApJ*, 565, 773
- Tokunaga, A. T., Sellgren, K., Smith, R. G., Nagata, T., Sakata, A., & Nakada, Y. 1991, *ApJ*, 380, 452
- Vanden Berk, D. E., et al. 2001, *AJ*, 122, 549
- Vaughan, S., & Fabian, A.C. 2004, *MNRAS*, in press (astro-ph/0311473)
- Veilleux, S., Kim, D.-C., & Sanders, D. B. 1999, *ApJ*, 522, 113
- Veilleux, S., & Osterbrock, D. E. 1987, *ApJS*, 63, 295
- Véron-Cetty, M.-P., Woltjer, L., Staveley-Smith, L., & Ekers, R. D. 2000, *A&A*, 362, 426
- Vignali, C., Brandt, W. N., & Schneider, D. P. 2003, *AJ*, 125, 433
- Vignati, P., et al. 1999, *A&A*, 349, L57
- White, R. L., et al. 2000, *ApJS*, 126, 133
- Wilkes, B. J., Schmidt, G. D., Cutri, R. M., Ghosh, H., Hines, D. C., Nelson, B., & Smith, P. S. 2002, *ApJ*, 564, L65
- Wilkes, B. J., Tananbaum, H., Worrall, D. M., Avni, Y., Oey, M. S., & Flanagan, J. 1994, *ApJS*, 92, 53
- Wills, B. J., Netzer, H., & Wills, D. 1985, *ApJ*, 288, 94
- Wisotzki, L., Koehler, T., Groote, D., & Reimers, D. 1996, *A&AS*, 115, 227
- Yuan, W., Brinkmann, W., Siebert, J., & Voges, W. 1998, *A&A*, 330, 108
- Yuan, W., Siebert, J., & Brinkmann, W. 1998, *A&A*, 334, 498
- Zamorani, G., et al. 1981, *ApJ*, 245, 357